Materials Today Advances 12 (2021) 100184

Contents lists available at ScienceDirect

Materials Today Advances

journal homepage: www.journals.elsevier.com/materials-today-advances/

Novel in situ multi-level analysis of structural-mechanical relations in a bioinspired polyurethane-based tissue model

Jingyi Mo [a, **], Nathanael Leung [a], Priyanka Gupta [b, c], Bin Zhu [a], Eirini Velliou [b, c], Tan Sui [a, *]

[a] Bioinspired Materials Group, School of Mechanical Engineering Sciences, University of Surrey, Guildford, Surrey, GU2 7XH, UK
[b] Bioprocess and Biochemical Engineering Group (BioProChem), Department of Chemical and Process Engineering, University of Surrey, Guildford, Surrey, GU2 7XH, UK
[c] Centre for 3D Models of Health and Disease, Division of Surgery and Interventional Science, University College London, London, W1W 7TY, UK

ARTICLE INFO

Article history:
Received 1 September 2021
Received in revised form
22 October 2021
Accepted 26 October 2021
Available online 2 November 2021

Keywords:
Bioinspired polyurethane
Surface functionalisation
Synchrotron X-ray scattering techniques
Confocal laser scanning microscopy
In situ micromechanical testing
Pancreatic cancer
Cancer cells
3D scaffolds
Extracellular matrix (ECM)
Collagen
Fibronectin

ABSTRACT

In this manuscript, we elucidated, for the first time, the substructural mechanisms present in our recently developed bioinspired polyurethane-based pancreatic tissue models. Different protein coatings of the model, i.e., collagen and fibronectin were examined. More specifically, analysis took place by combined real-time synchrotron X-ray scattering techniques and confocal laser scanning microscopy, to quantify the structural alteration of uncoated-polyurethane (PU) and protein-coated PU as well as the time-resolved structural reorganisation occurring at the micro-, nano- and lattice length scales during in situ micromechanical testing. We demonstrate that a clear increase of stiffness at the lamellar level following the fibronectin-PU modification, which is linked to the changes in the mechanics of the lamellae and interlamellar cohesion. This multi-level analysis of structural-mechanical relations in this polyurethane-based pancreatic cancer tissue model opens an opportunity in designing mechanically robust cost-effective tissue models not only for fundamental research but also for treatment screening.

1. Introduction

Pancreatic Ductal Adenocarcinoma (PDAC), the 14th most frequent malignancy worldwide, is a highly devastating cancer with unmet clinical needs. Once metastasised, prognosis for PDAC is extremely poor with a 5-year survival rate less than 8% and an average life expectancy of 4–6 months [1]. Such a low survival rate has barely been improved since the 1970s [2,3]. These dismal statistics are mainly attributed to the lack of distinctive biomarkers for early-stage detection, rapid and aggressive metastasis along with a complex tumor microenvironment (TME) which facilitates resistance for therapeutic treatment and even recurrence [4–6].

Advancements in the field of tissue engineering have attracted cancer researchers with the hopes of developing *in vitro* tissue-engineered models for observing the physiological process of cancer evolution and treatment responses. Although conventional two-dimensional (2D) tissue models are low-cost, easy to use, and reproducible in approach, they fail to simulate the native features of TME, such as three-dimensional (3D) structure of TME, cellular spatial distribution and environmental gradients, which are imperative to response of therapeutic treatments [7–14]. Animal models, e.g. mice, allow for more realistic cellular interactions *in vivo*, and have therefore been widely applied for chemo-radiotherapy testing at selected stages of disease. However, many therapeutic treatments that cure cancer in mice have limited effectiveness and reliability in humans due to foreign physiology [7,8,15–18].

The emerging 3D tissue models have become a promising alternative to 2D tissue models and animal models. Important criteria for designing 3D tissue models include appropriate porosity

* Corresponding author.
** Corresponding author.
E-mail address: t.sui@surrey.ac.uk (T. Sui).

https://doi.org/10.1016/j.mtadv.2021.100184

and interconnectivity, for facilitating cellular spatial organisation, and adequate surface properties, for hosting cell attachment and anchorage [19–21]. Mechanical strength is equally important as mechanical cues can modulate the cellular cross-talk and cell-Extracellular Matrix (ECM) interactions [22,23]. In an attempt to develop 3D tissue model systems, polyurethane (PU) draws special interests due to its low cost, excellent mechanical properties, ease of manufacturing, and decent biocompatibility, along with its' relatively high stiffness, which is a typical characteristic of pancreatic cancer tissues [13,18]. Moreover, the biochemical and biomechanical features of PU-based tissue models can be tailored by surface modifications with different ECM protein such as collagen (Col) and fibronectin (FN), to reproduce a 3D TME that can ensure the cell–cell and cell–matrix interactions [18,24–26]. These complex interactions play a key role in the progression of the disease, its metastasis as well as its response to treatment options. Recapitulating those interactions in 3D can mimic more accurately what happens *in vivo*.

However, as a material, PU may undergo deterioration, under certain device-specific conditions. For instance, cellular activities or loading conditions might have significant impacts on the development of mechanical degradation. This impairs the mechanical stability of PU and consequently may lead to catastrophic failure [27,28]. Understanding the relation between the internal structure, mechanical properties and their response to cellular growth, and self-organisation is essential to the design strategies that can lead to a very substantial improvement in effectiveness and reliability on the design of *in vitro* tissue-engineered models.

Whilst the gross mechanical behaviour of PU-based tissue models has been well characterised at the macroscopic scale, the mechanical properties at the micro-, nano- and finer scales, which have been reported to be detrimental to the efficiency of drug delivery into tumors, have been neglected [12,13,18,29,30]. The current study combines, for the first time, real-time synchrotron X-ray techniques (Small-and Wide- Angle X-ray Scattering, SAXS and WAXS) and microanalysis methods (confocal laser scanning microscopy, CLSM) to investigate the structural reorganisation and mechanical properties of this PU-based tissue model in response to surface modification by ECM protein occurring at multiple length scales during mechanical loading. Consequently, such novel analytical approach can help build a more detailed understanding of the structural optimisation strategies at different length scales [31–34]. This provides an observational basis for improved insight into the structure-property relations for future design and development of the *in vitro* tissue-engineered model and its application in both bioengineering but also in biomedicine such as the evaluation of therapeutic treatment [13].

2. Materials and methods

2.1. Sample preparation

2.1.1. Polymer scaffold preparation and surface modification

PU beads (EG-80A, Noveon, Belgium) were dissolved in organic solvent dioxane (5% w/v) (99.8% anhydrous pure, Sigma-Aldrich, UK) then quenched at −80 °C for 3 h followed by solvent removal by freeze drying in a poly-ethylene glycol (PEG) bath at −15 °C. The scaffolds were then cut into 5 × 10 × 2.5 mm^3 cubes. They were then sterilized by dipping them in 70% ethanol (3 h) followed by UV ray exposure (1 h). As previously reported, the average pore size of the scaffolds was 100–150 μm and the porosity was 85–90% [19,35]. The chemical components of PU discussed in this paper consist of poly (tetrahydrofuran) (pTHF), as a soft segment (SS) in combination with a hard segment (HS) (hexamethylene diisocyanate (HMDI) and 1,4-butanediol (chain extender)).

As previously described [12–14,36], the generated scaffolds were surface modified (adsorption) with fibronectin (Sigma-Aldrich, UK) and collagen I (Sigma-Aldrich, UK) for ECM mimicry. Briefly, the scaffolds were centrifuged in Phosphate Buffered Saline (PBS, Sigma-Aldrich, UK) for 10 min at 2500 rpm, followed by further centrifugation in fibronectin/collagen I solution (25 μg ml^{-1}) for 20 min at 2000 rpm. A final centrifugation in PBS for 10 min at 1500 rpm was carried out to unblock the scaffold pores.

2.1.2. Cell culture on PU-based scaffolds

The 3D cell culture was conducted as previously described [14,36]. The human pancreatic adenocarcinoma cell line PANC-1 (Sigma-Aldrich, UK) was expanded in Dulbecco's modified Eagle's medium (DMEM) with high glucose (Lonza, UK) supplemented with 10% fetal bovine serum (Fisher Scientific, UK), 1% penicillin/streptomycin (Fisher Scientific, UK) and 2 mM L-glutamine (Sigma-Aldrich, UK) in a humidified incubator at 37 °C with 5% CO_2. For all experimental conditions, 2 × 10^6 cells (re-suspended in 30 μl of cell culture media) were seeded in each scaffold. Immediately after seeding, the scaffolds were placed in the incubator for 1 h to promote cellular attachment within the scaffolds. Thereafter, 1.5 ml of cell culture media was added to each scaffold followed by incubation in a humidified incubator at 37 °C with 5% CO_2 for the entire duration of the experiment (2 weeks). The cell culture medium was changed every two days. At the end of the culture period, the scaffolds were fixed with 4% paraformaldehyde (SIGMA- Aldrich, Merck, UK), dried in a vacuum desiccator for further imaging and analysis. Uncoated PU scaffolds were used as control for all experiments.

2.2. In situ confocal laser scanning microscopy

A customised tensile micro-device was designed to apply tensile deformation manually to PU scaffold with an accuracy of 0.1 mm. The position of the sample grip was adjusted till each specimen was straightened. The specimen length (distanced between two sample grips) was determined using caliper with an accuracy of 0.1 mm. PU scaffold was subsequently secured on this test rig which can be placed onto the laser scanning confocal microscope (CLSM) (Ti-Eclipse Inverted Microscope System, Nikon Instruments Europe) equipped with solid-state lasers for excitation. Specimens were excited using a 355 nm laser and fluorescence was detected at 457 nm. Images were acquired under × 10 magnification objective lens with a DS-Qi1 camera, as z-stacks with 1 μm intervals. The gross strain was applied to PU specimen at the strain level of 0%, 50%, 100% and 170%. At each strain increment, the fluorescence image was refocused before the nuclei of cell was recorded. With the images at different strain increment, the relative displacement between cell nuclei in the loading direction was analysed and measured by ImageJ [37], as described in *Supplementary material*.

The relative displacement of 15 pairs of cells was examined for each treatment.

2.3. In situ micromechanical testing with SAXS/WAXS

The nano- and atomic mechanics of the PU specimens were probed through in situ synchrotron SAXS/WAXS experiment at the B16 beamline at Diamond Light Source (DLS, UK). PU specimens loaded on the micro-mechanical testing rig (Microtest, Deben Ltd., Suffolk, UK) were stretched at a constant extension rate of 0.2 mm/min. A 200 N load cell enabled load parameters to be recorded throughout the experiment. The experimental configuration is depicted in Fig. 1. The SAXS and WAXS patterns (wavelength 0.6890 Å) were acquired during the mechanical loading with an acquisition interval of 0.2 N. WAXS patterns were acquired with an Imagine Star 9000 detector (Photonic Science Ltd., UK) with a 500 ms exposure time (sample-detector-distance: 85.8 mm). SAXS patterns were collected with Pilatus 300k detector (Dectris, Baden, Switzerland) right after the WAXS measurement with a 200 ms exposure time (sample-detector-distance: 1780 mm).

2.4. Data processing and analysis

2.4.1. SAXS lamellae long period

For polymer, the scattering signal was resulted from the frequently occurring spacing of semi-crystal and amorphous lamellae stacks. An example of two-dimensional (2D) SAXS patterns, shown in Fig. 1 (A1), was integrated azimuthally over the angular range (χ) of $\pm 20^{\circ}$ straddling the loading direction using Fit2D [31,38]. The resultant 1D radial intensity profile (Fig. 1 (A2)) was subsequently converted from reciprocal space to real space dimension using the electron density function ($\gamma(x)$) as follows:

$$\gamma(x) = \int_0^{\infty} I(q) q^2 \cos(qx) \mathrm{d}q \Big/ \int_0^{\infty} I(q) q^2 \mathrm{d}q \tag{1}$$

The peak position corresponding to the average value of lamellae long period (L_P) is denoted by the red arrow in Fig. 1 (A3) and was further determined to be ~10 nm via Gaussian function fitting. The percentage changes of L_P with respect to its unstretched

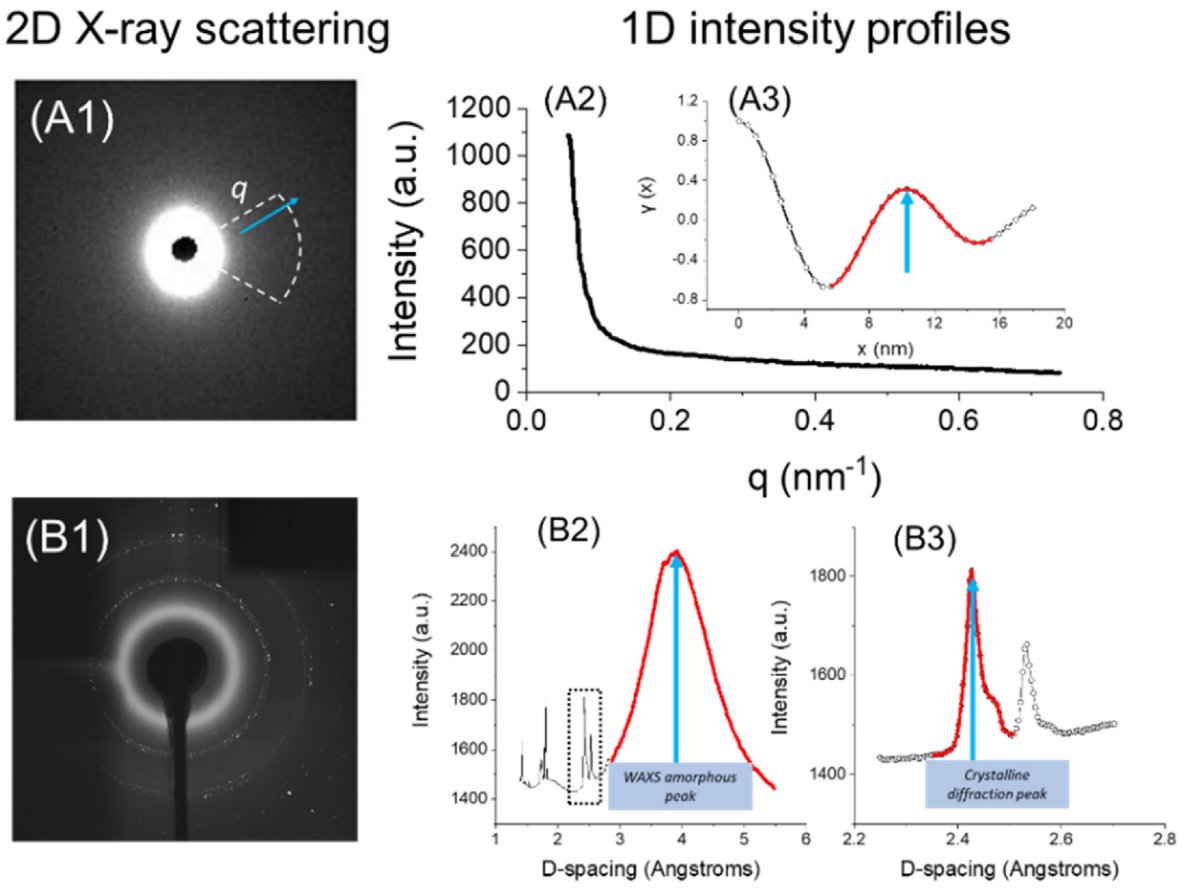

Fig. 1. X-ray data reduction pipeline: (A1) Representative 2D SAXS patterns from PU scaffold. (A2) A dotted line denotes the area where the azimuthal averaging of intensity was performed. (A3) The electron density function of PU scaffold with the peak position corresponding to the lamellae long period at ~10 nm, denoted by blue arrow. (B1) An example of 2D WAXS pattern from PU scaffold. (B2) A 1D WAXS intensity profile. (B3) Enlarged plot of the highlighted in the rectangular area shown in (B2). The crystalline diffraction peak, denoted in blue arrow, was fitted to determine the WAXD strain.

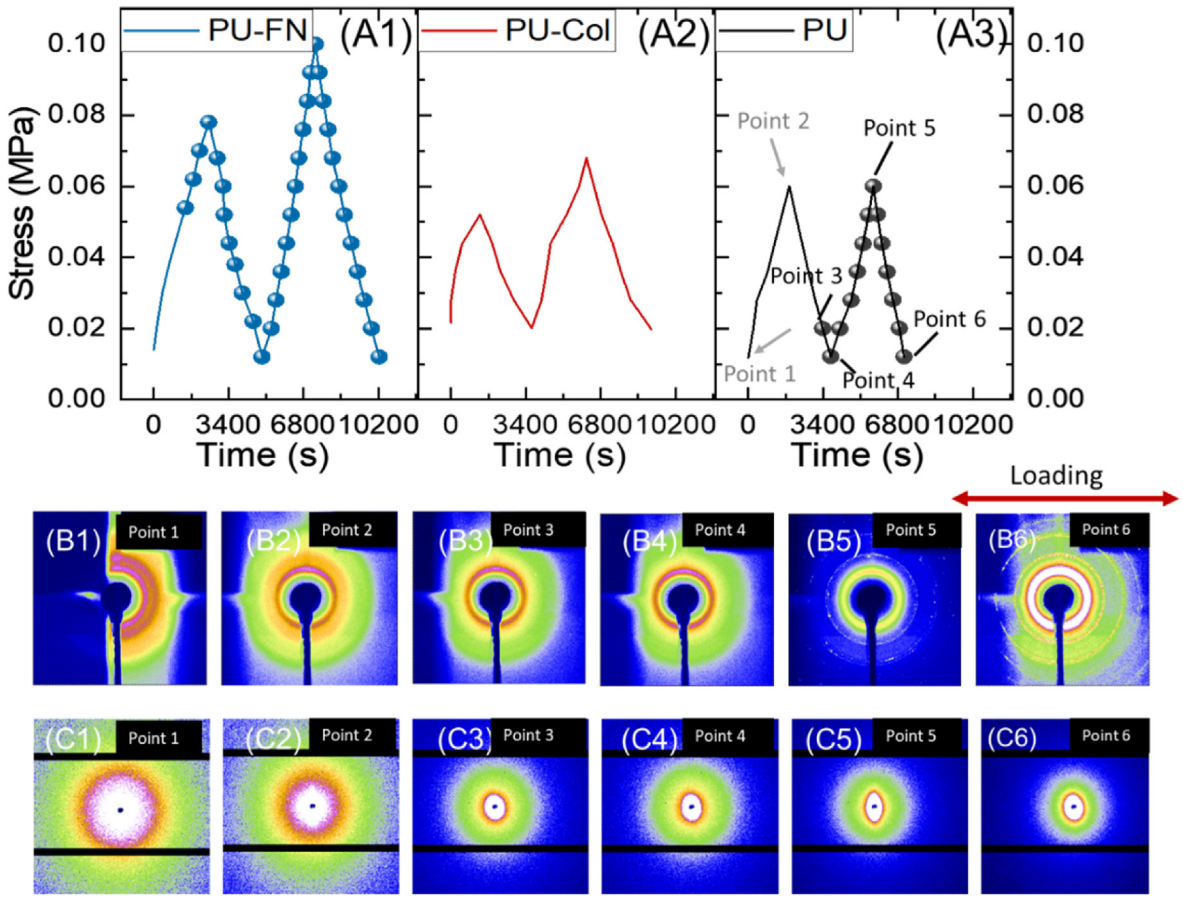

Fig. 2. (A1, A2, A3) stress vs. time plots for PU-FN, PU-Col and uncoated-PU specimens. Data points where crystallisation occurred are highlighted with solid spheres. 2D WAXS (B1–B6) and 2D SAXS patterns (C1–C6) correspond to the data points 1–6 indicated in (A3).

state can be considered as a strain gauge at the lamellar scale.

2.4.2. WAXS lattice strain

Each 2D WAXS pattern was integrated azimuthally across an angular range of ±20° (Fig. 1 (B1)), resulting in a 1D WAXS intensity profile as a function of lattice d-spacing $I(D)$. The resultant 1D profile is presented in Fig. 1 (B2). The lattice strain (WAXS strain, ε_{WAXS}), indicating the structural evolution at the atomic scale was calculated from the percentage changes of peak centre position at ~2.4 Å with respect to the unstrained state as a reference. The amorphous halo corresponds to the overlying reflection of the urea moieties [39].

2.4.3. Degree of crystallinity

The degree of crystallinity was calculated from the ratio of the crystalline diffraction intensity (Ic) to the overall scattering intensity (I_{waxs}) comprised of amorphous intensity (Ia) and Ic [32].

$$\text{Crystallinity} = \frac{I_c}{I_{waxs}} \times 100 = \frac{I_c}{I_c + I_a} \times 100 \quad (2)$$

2.4.4. 2D SAXS and WAXS patterns evolution during deformation

The evolution of SAXS patterns of the uncoated PU specimen during uniaxial loading is presented in Fig. 2 (A). SAXS patterns of uncoated PU specimen first converts from circular ring to rounded ellipse form during the first loading cycle from point 1 to point 2. Subsequently, the elliptical form was observed to become narrower after reloading to point 5. The preferred orientation is aligned to the loading direction (i.e. horizontal direction in real space), corresponding to the short axis of the elliptical patterns (reciprocal space). The corresponding WAXS patterns in Fig. 2 (B) are completely isotropic with a broad amorphous halo in the early state of the deformation. To highlight the differing strain-induced-crystallisation (SIC) onsets by differing surface functionalisation, the stress-time curves were plotted for uncoated-PU (black), PU-Col (red) and PU-FN (blue) in Fig. 2, with solid spheres indicating where the crystal phase starts forming, as observed from the occurrence of diffraction rings in WAXS patterns. The diffraction peaks at D-spacings of 1.9 Å and 2.4 Å were believed to be as a result of the strain-induced crystalline pTHF and HS, as had been reported elsewhere [33,40]. The required minimum strain to observe crystallisation in PU-FN is ~100% after approximately 1700 s in the first

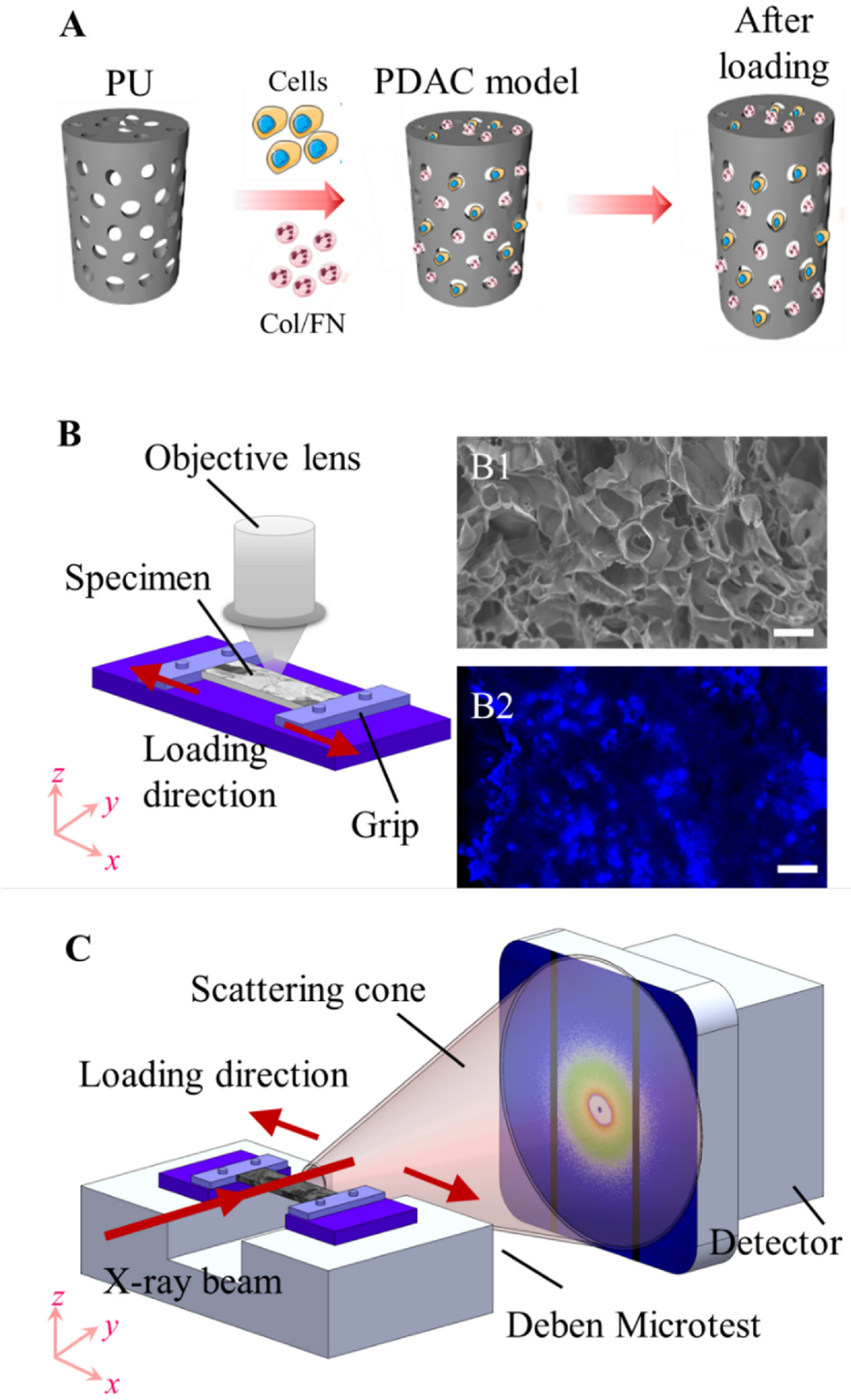

Fig. 3. (A) Schematics of the development of the PU-based tissue model for PDAC. Prior to tensile loading, PU scaffolds were surface modified with collagen and fibronectin and seeded with pancreatic cancer cells, which were left to grow for 2 weeks prior to the mechanical analysis. (B) Schematics of the micromechanical experimental configuration. In a

loading phase. The uncoated-PU shows crystallisation later in the first cycle (~3200 s) upon unloading. By reaching the critical SIC onset strain, the crystallisation is found to be persistent throughout the two-cycle deformation for both uncoated-PU and PU-FN, while no crystallinity was observed in PU-Col during the deformation.

3. Results and discussions

The method to fabricate the pristine polymeric polyurethane (PU) scaffolds took place as previously described [13,14]. As shown in Fig. 3 (A), the PU scaffolds were firstly surface functionalised with ECM protein including FN and Col, as previously described, prior to the 3D cell culture for two weeks (human pancreatic adenocarcinoma cell line PANC-1 [13]. The sample selection consisted of the following three groups: i) uncoated-PU; ii) PU coated with collagen (PU-Col); iii) PU coated with fibronectin (PU-FN).

Strain-controlled tensile tests of PU scaffolds were performed using a micro-device and adapted to a Nikon inverted confocal microscope (Nikon Instruments, Europe) as shown in Fig. 3 (B) based on our previous findings [12,14], when seeding 500,000 cells we can see very dense cell aggregates after 4 weeks in culture. For time optimisation of our experiments we therefore increased the seeding density to 2,000,000 which lead to a similar effect after 2 weeks as can be seen in Fig. 4. Significantly higher numbers of PANC-1 cells were observed on ECM protein coated (FN and Col) PU scaffolds relative to those uncoated ones with FN coating resulting in maximum cell growth and dense and homogeneous cell aggregate formation, in accordance with our previous results (Fig. 4 (C)). [13,14]. When looking at the macroscopic strain, our results revealed that cells on scaffolds with different surface modification – uncoated-PU (black), PU-Col (red) and PU-FN (blue) – display a differing extent of extension at the same macroscopic strain ε_M. At a given macroscopic strain ~100%, cells in PU-Col had a much larger elongation of 72.2 ± 7.6% as compared with uncoated-PU (37.1 ± 12.0%). The reduced cellular strain observed in PU-Col is possible due to the reduced stiffness of cell which has been reported to be closely related to the reduction of defined actin fibre networks and a looser cytoskeleton structure [41–43]. Integrins are cell adhesion receptors which undergo cell type-specific regulation of adhesive capabilities: different cell types use different integrins to bind to substrates with different ECM proteins [44,45]. In our case, similar to other cell types/cell lines, PANC-1 cells use different integrins to bind to Col and FN respectively. These different integrins play a key role in sensing the matrix protein, signalling transduction pathway, and possibly result in changes in the actin filament arrangement of the cells which then effect cell stiffness. Furthermore, the cellular strain was much lower in PU-FN (20.3 ± 40.00%). It is noted that the averaged cellular strain scaffold increased linearly with the applied macroscopic strain, but with noticeable error bars. This phenomenon was most obvious in the case of PU-FN group, where there was a greater standard deviation in comparison to the other two groups. The structural reason for this is local heterogeneity in stiffness, very likely introduced by the conformational changes in interlamellar entanglement, strain-induced-crystallisation and other phenomena [46,47]. Under tensile deformation, the soft segment elongates mainly whilst the hard-crystalline segment scarcely does. The interlamellar crosslinks in conjunction with the crystallisation process in the proximity of crosslinks will lead to an inhomogeneous strain field depending on the local segmental stiffness under deformation, resulting in a more dispersed cellular displacement measured by in situ CLSM in PU-FN.

The in situ synchrotron SAXS/WAXS measurements of PU scaffolds were carried out at the beamline B16 in Diamond Light Source (DLS, UK), as shown in Fig. 5 (C). The multiple length-scale strain evolution over the entire loading history is plotted in Fig. 5 (A-C), including the macroscopic strain, measured using a Deben Microtest rig (Deben, UK), and nano-scale strain, extracted from the SAXS patterns. Under tension, we observed significant strain-induced crystallisation in uncoated-PU and PU-FN, while no crystallinity was found in PU-Col. Hence, only the evolutional changes of lattice strain and crystallinity for uncoated-PU and PU-FN measured from the diffraction signal of the WAXS pattern are presented in Fig. 5 (C, D). The intrinsic mechanical behaviour of uncoated-PU (black), PU-Col (red) and PU-FN (blue) at macro-scale are depicted in Fig. 5 (A), showing classical non-linear stress-strain curves of polymeric material. In loading cycle #1, the macroscopic stress σ_M with strain ε_M at ~160% for PU-FN specimen (0.064 MPa) is much higher than PU-Col (0.030 MPa), whereas the uncoated-PU specimen (0.032 MPa) is between the other two groups. It is also worth noting that the slope of the stress-strain curves increased and tensile residual strain appeared in both uncoated-PU and PU-FN, indicating the strain-induced crystallisation as manifested by the diffraction signal appearing in the WAXS patterns observed in Fig. 2. No apparent changes can be identified in PU-Col mechanically over the entire loading history. Fig. 5 (B) shows the corresponding macroscopic stress (σ_M) vs. lamellar (ε_l, measured from SAXS patterns) for uncoated-PU (black), PU-Col (red) and PU-FN (blue). The results revealed that the soft lamellae in PU scaffold with different surface modifications – PU-Col, uncoated-PU, and PU-FN – show a differing extent of extension at the same macroscopic stress σ_M. It is found that the uncoated-PU and PU-FN displays lower lamellar strain at the same macroscopic stress alongside with steady increase in stress/lamellar strain relative to PU-Col. The stiffening effect introduced by FN was found to be most prominent, comparing the loading slopes of uncoated-PU and PU-FN at macro- and nano-scale as shown in Fig. 5 (A-B), which could be attributed to the increased interlamellar cohesion promoted by FN fibrils. Considering that significant strain-induced crystallisation occurred in uncoated-PU and PU-FN, the lamellar extensions (ε_l) in these two groups may further be constrained due to the 'self-reinforcement' led by the formation of hard phases during the deformation. It is also noted that the Col-modification lowers the tensile properties of PU scaffold throughout the entire loading history. In terms of WAXS strain (lattice scale), it is found that the surface modification by FN produced larger increases in lattice strain at maximum stress throughout the entire loading history. Furthermore, it is noted that the degree of crystallinity for PU-FN increases gradually along with loads (Fig. 5 (D)).

The foregoing results can be quantified as follows. The differences of surface modification in uncoated-PU, PU-Col and PU-FN led to changes of maximum tangent modulus and maximum lamellar strain (Fig. 6 (A, B)). The maximum tangent modulus of PU reduced dramatically by 40% from 0.23 ± 0.17 MPa in uncoated-PU

bespoke micro-device mounted on a confocal laser scanning microscope stage, the nucleus of cell is visualised by DAPI staining (B2), allowing the strain measurement from cellular displacement tracking during tensile loading along *x*-axis. Scale bar = 100 μm. (C) Schematics of the nano- and lattice scale experimental configuration. In a Deben Microtest rig mounted on the sample stage of a synchrotron beamline, time-resolved SAXS and WAXS measurements were performed to quantify the structural changes of PU scaffold in response to tensile load.

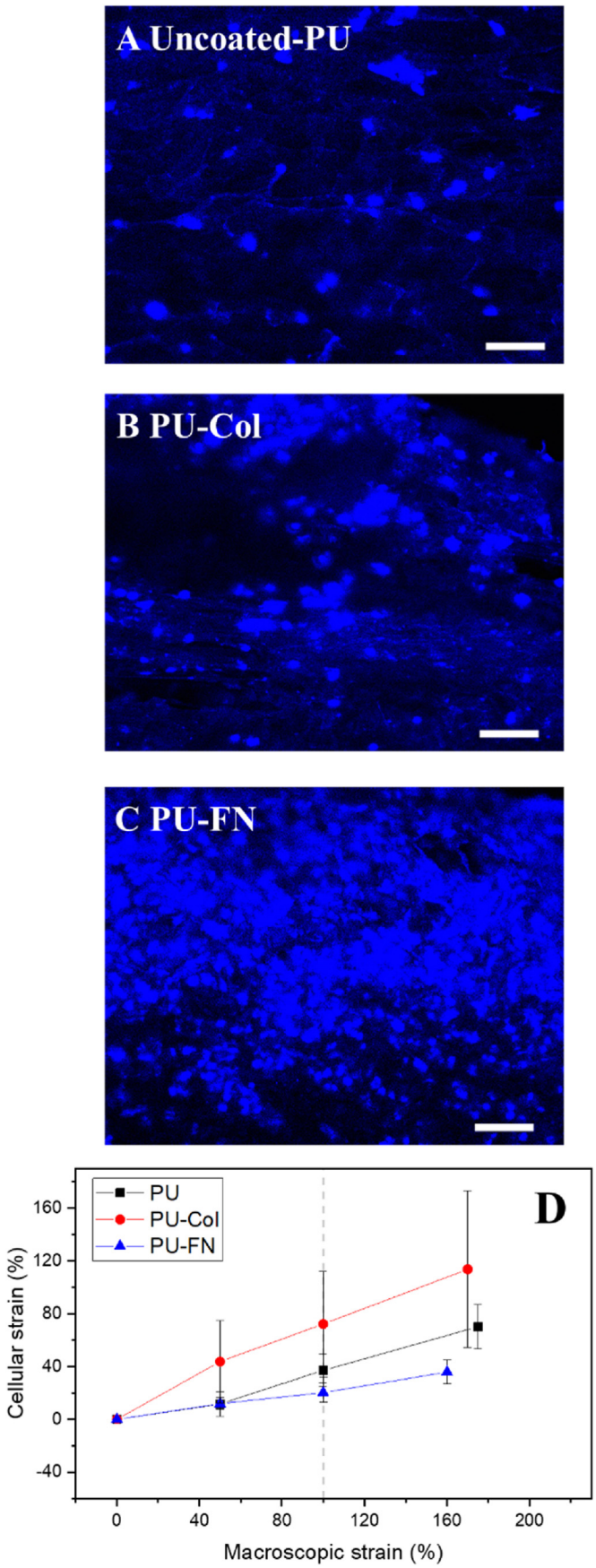

to 0.13 ± 0.06 MPa after surface-modified with Col, whilst the maximum tangent modulus was ~four times larger after surface-modified with FN (0.58 MPa) relative to PU-Col. Similarly, the nano-scale parameter lamellar strain showed clear differences between groups, with maximum lamella elongation developed in control uncoated-PU (0.34 ± 0.02%) and stiffened PU-FN (0.32 ± 0.03%) where apparent strain-induced crystallisation (SIC) is observed being much less (~35%) compared with softened PU-Col (0.47 ± 0.03%). Concurrently, the fraction of the deformation take-up in lamellar level (the ratio of lamellar strain to macroscopic strain, $\varepsilon_l/\varepsilon_M$) exhibited an increasing trend from surface-modified groups to uncoated group (Fig. 6 (C)), with a ratio ($\varepsilon_l/\varepsilon_M$) of 0.0066 in softened PU-Col being 30% larger than that from control un-coated-PU (0.0046), and further increased to 0.031 after treatment with FN. Such an increase of strain take-up in PU-FN dictated that there was increased load borne and transferred through the structural units at each length scale during the tensile loading compared with uncoated-PU and PU-Col, possibly due to the effect of increased interlamellar cohesion produced by FN. At the lattice scale, the degree of crystallinity follows the same increasing trend as tangent modulus in Fig. 6 (A). Compared to uncoated-PU (0.8 ± 1.0), the crystallinity of PU-FN exhibits a significant increase of approximately four folds (2.9 ± 0.3). The elevated crystallinity in PU-FN compared to uncoated-PU leads to an evident increase of mechanical tensile properties since the segmental soft lamellae motion is reduced due to the formation of rigid crystal phases. The magnitude of variation in macroscopic mechanical properties such as tangent modulus for the whole PU specimens for all treatments (uncoated-PU, PU-Col and PU-FN) is much greater compared with the strain developed at the lamellar level (Fig. 6 (B)), indicating that surface properties such as interlamellar entanglements and cohesion are also important in the stiffening of PU scaffold (see Fig. 7).

To better explain our experimental observations, a conceptual model that sheds light on the key biophysical mechanisms enabling mechanically tuneable PU is proposed in Fig. 5. The uncoated-PU, PU-Col and PU-FN are shown in grey, red and blue, respectively. At the nano-scale, PU scaffold can be considered as a two-phase nanostructured material comprised of an anisotropic phase (soft lamellae) separated by a rubbery phase with relatively higher extensibility (interlamellar matrix). The interconnections between lamellae modulated by surface modification can be considered as a measurement of interlamellar cohesion/entanglement. In the case of PU-FN, the coiled chains in the interlamellar matrix bind to two adjacent lamellae in the unstressed state, forming a low-stiffness entangled interlamellar network which connects the high-stiffness lamellae. Under tensile straining, the stiffness mismatch between the stiffer lamellae and softer interlamellar matrix will lead to an inhomogeneous strain field. In this strain field, tensile loads developed in the lamellae and matrix, with significant shear forces occurring in the matrix surrounding lamellae. The increased interlamellar entanglements and cohesion led by FN fibrils could be considered as 'load-transmitters', resulting in the shear force being transferred more effectively between the lamellae (Fig. 7). Under tensile deformation, small alterations in the mechanical properties of the interlamellar matrix could be amplified to considerable changes in macroscopic stress, as a result of the of increase lamellar recruitment to bear loads, not due to the stresses carried inside the matrix. The increased efficiency of shear load conferring is supported by a greater lamellar strain take-up in PU ($\varepsilon_l/\varepsilon_M$ = 0.03 as

Fig. 4. Representative fluorescence CLSM images of sections of the 3D PU scaffold culturing PDAC cancer cells in (A) uncoated PU, (B) Col coated PU and (C) FN coated PU. Cells are stained by DAPI showing blue fluorescence. Scale bar = 100 μm. (D) cellular strain vs. applied microscopic strain from PU scaffold surface modified by Col and FN.

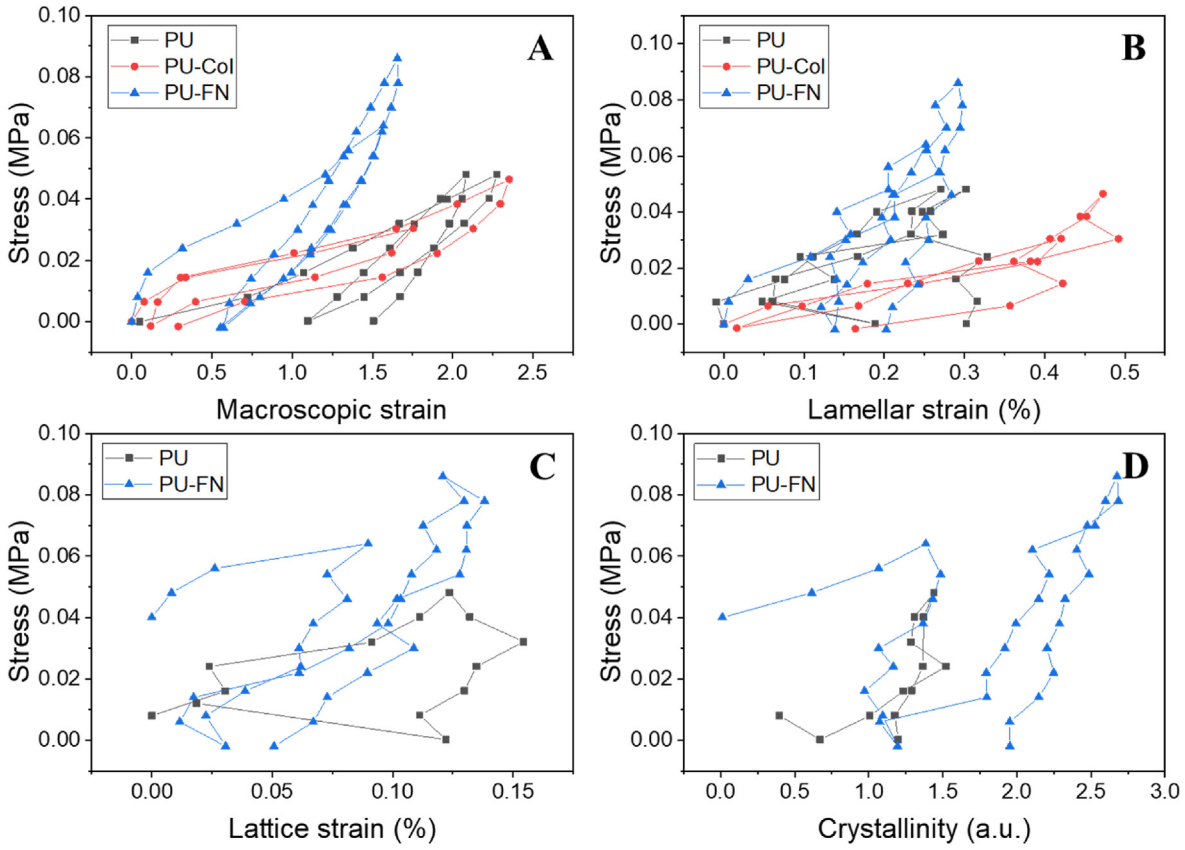

Fig. 5. (A) Macroscopic stress vs. strain plots for uncoated-PU, PU-Col and PU-FN during loading, showing clear differences in terms of tangent modulus and maximum stresses. (B) Corresponding Macroscopic stress vs. lamellar strain measured from the changes of lamellar long period during loading. Structural units at lamellar level exhibited higher resistance to deformation in uncoated-PU and PU-FN, compared to PU-Col. (C, D) Corresponding Macroscopic stress vs. lattice strain and crystallinity measured from diffraction peaks from PU with different surface modifications. No crystalline structure was found in PU-Col hence only uncoated-PU and PU-FN were plotted.

shown in Fig. 6 (C)). On the other hand, a significant decrease of $\varepsilon_l/\varepsilon_M$ is observed in PU-Col compared to PU-FN. Such a reduction in strain ratio complements a decreased interlamellar cohesion and load-bearing capacity after Col-modification, which in return supports the claim that the interlamellar interconnection. Different fabrication methods will lead to a differing strain ratio: for example, the strain evolution from macro-to nano-scale for electron spun PU ($\varepsilon_l/\varepsilon_M$ = ~0.3) [32,33], which is about 10 times greater than the value we found in our freeze-casted PU. To modify the mechanical properties of PU, in general, there are two distinct methods: either by alteration of the mechanics of the lamellae itself or by modulation of interlamellar cohesion. The strain-induced crystallisation is a thermodynamic process, triggered by a reduction in entropy of the polymer system as they are getting stretched [49,50]. The crystallinity in PU-FN is relatively higher than uncoated-PU, which implies the molecular chains can be deformed and reoriented more effectively, enabling more chains to crystallise along the loading direction. Similar phenomenon has been reported in the system of crosslinked natural rubber [51]. Increasing the amount of crystalline phase will lead to an increased lamellar modulus, which is further supported by the observation of reduced ε_l in uncoated-PU and PU-FN compared to PU-Col. Therefore, it can be concluded that the enhanced mechanical properties observed in PU-FN are associated with the combined effects of an alteration of the interlamellar cohesion due to surface modification and a self-reinforcement as a result of strain-induced-crystallisation. We have also evaluated the amorphous halo and found that even at the highest strain, the crystallinity in the system is less than 3% in uncoated-PU. This result means that at the lattice scale, the majority of molecules in the PU system is under the uncrystallisable condition and remains undeformed at high levels of strain. Only a minor portion is being recruited and crystallised.

4. Conclusion

We have used both real-time synchrotron X-ray techniques (SAXS and WAXS) and CLSM during the mechanical loading to reveal how the hierarchical architecture and mechanical performance of a PU-based scaffold tissue model depend on the interaction between the micro-, nano- and lattice scale components

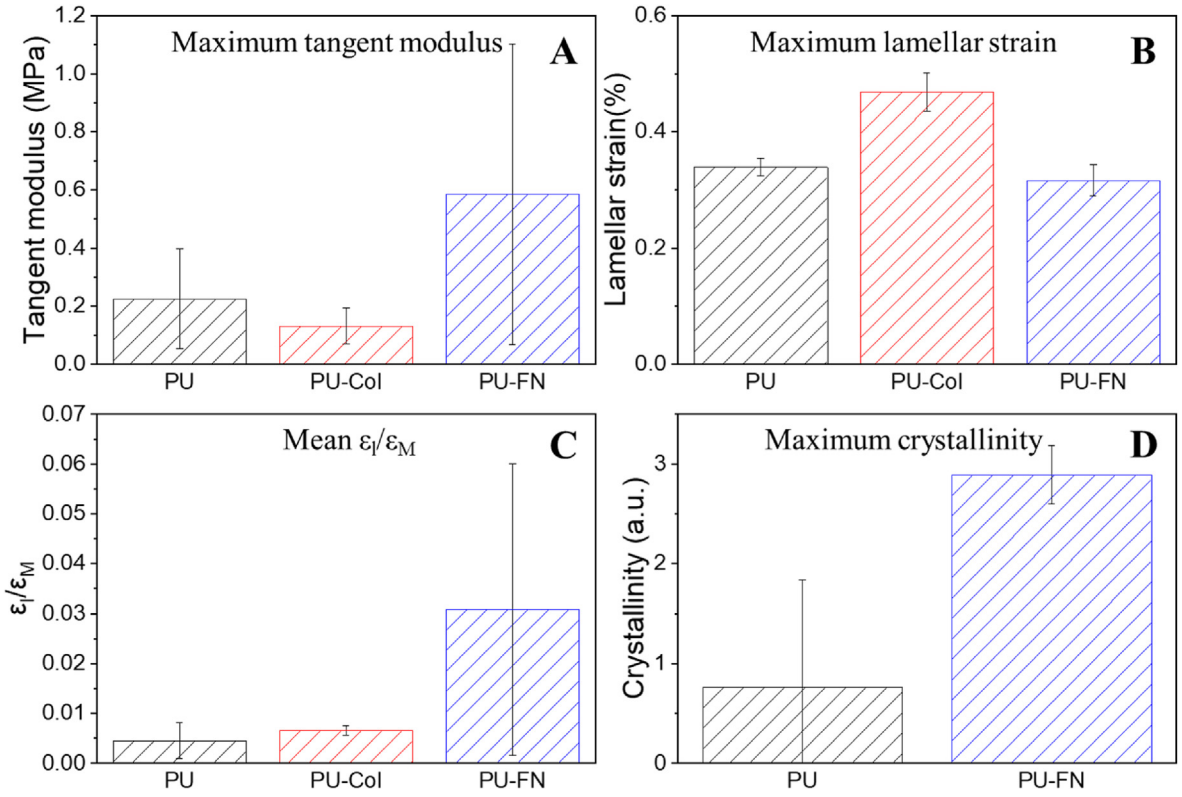

Fig. 6. (A) Averaged maximum tangent modulus for uncoated PU (black, n = 3), PU-Col (red, n = 3) and PU-FN (blue, n = 3). Error bars are standard deviations. n denotes the number of PU specimens for each surface modification group. (B, C) At the lamellar level, maximum lamellar strain (B) and the mean ratio of lamellar strain to macroscopic strain for PU with different treatment. (D) Maximum crystallinity measured from WAXS diffraction peak for uncoated-PU and PU-FN.

under different surface modification conditions. By measuring the cellular displacement under tension, we found a decrease of cellular strain in PU-FN together with a greater error bar compared to PU-Col. Our results revealed a prominent effect of FN on density and stiffness of PADC cancer cell (Fig. 4). With regards to the greater error bar observed in cellular displacement of PU-FN, the underlying molecular mechanisms might be the structural irregularities and heterogeneities induced by strain-induced crystallisation, thereby results in a self-reinforcement of PU-FN.

The main findings are summarised as below:

1. Increased interlamellar cohesion at the nano-scale in PU-FN leads to nearly 3 folds increase in tangent modulus at the macroscopic level (Fig. 6). FN was found to be the optimal protein contributing to improved cell attachment and mechanical properties of PU scaffold. Col also showed a high degree of cell attachment compared to uncoated-PU but lowered the mechanical strength of PU scaffold compared to FN. The use of in situ synchrotron X-ray scattering techniques with combined micromechanical testing has allowed us to quantify the deformation mechanics at multiple length scales of PU surface-modified differently.
2. An altered lamellar deformation mechanics on FN-modification— reduced lamellar/macroscopic strain and increased interlamellar entanglement combined with increase macroscale tangent modulus.
3. A conceptual model suggests these effects arises from combined effects of the alteration in the interlamellar matrix properties as well as the lamellar modulus.
4. Whilst the biological mechanisms of the cellular cross-talk and the cell-ECM interactions in PU scaffold in response to FN and Col need to be further elucidated, we suggest that these changes at micro-, nano- and lattice scale level will shed lights on tailoring this bioinspired PU scaffold by combining both Col and FN to increase the ECM complexity biocompatibility and mechanical properties, and thereby design biochemically advanced 3D tissue-engineered scaffolds.

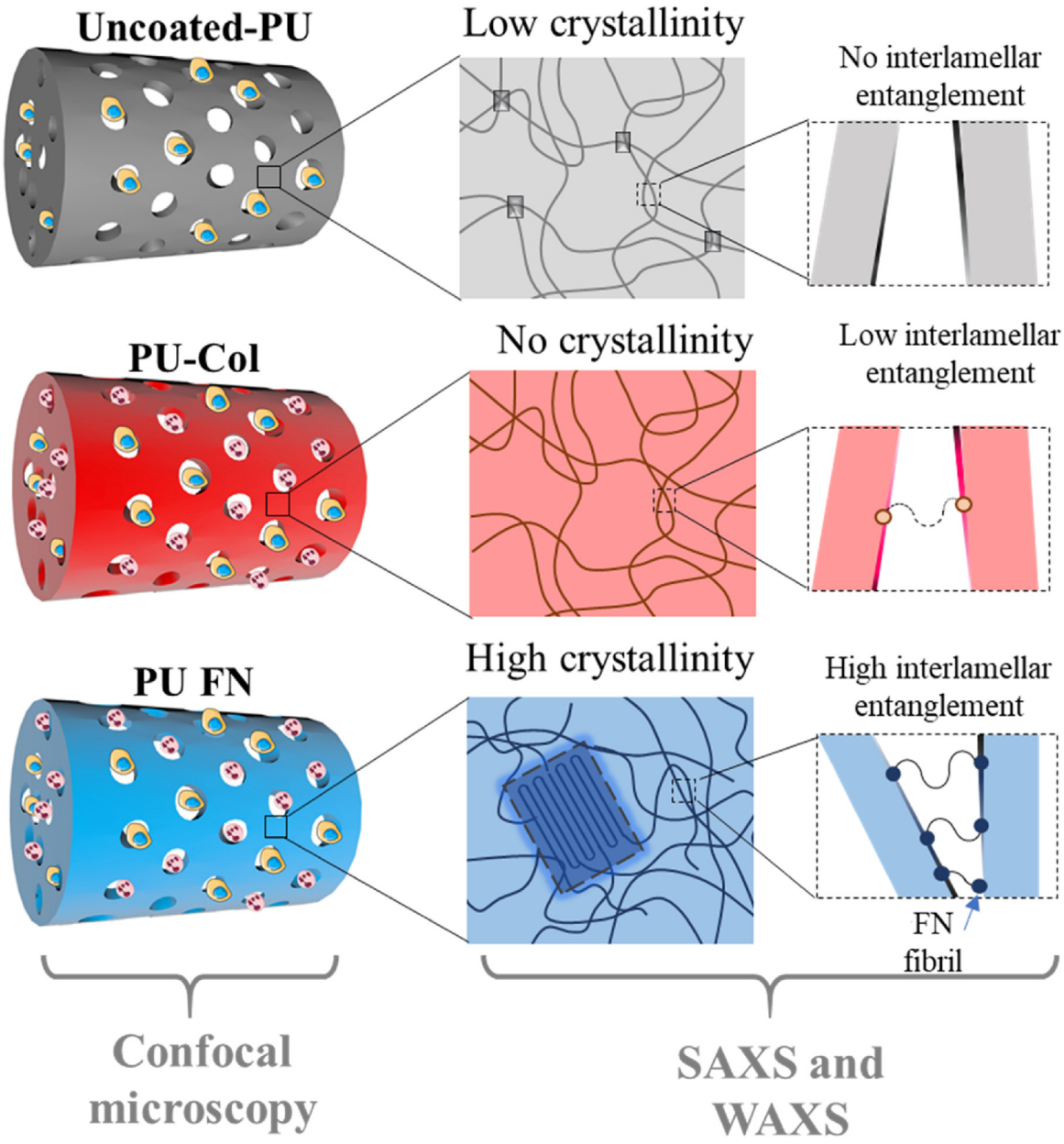

Fig. 7. Conceptual model of PU scaffolds with different surface modification treatments. At the micro-scale, pancreatic cancer cells are able to grow on PU scaffolds, with preferences of forming dense cell clusters in PU-Col and PU-FN. At the nano-scale, lamellae from uncoated-PU and PU-FN are self-reinforced by strain-induced crystallisation. In the zoom-in diagram showing the interactions between two adjacent lamellae, the interlamellar entanglements are further enhanced by FN-modification. The additive effects of self-reinforcement and interlamellar entanglements leads to the enhanced mechanical performance of PU-FN.

Declaration of competing interest

The authors declare that they have no known competing financial interests or personal relationships that could have appeared to influence the work reported in this paper.

Acknowledgements

We thank Dr Igor Dolbnya, from the B16 beamline at Diamond Light Source (DLS), for his support and assistance with experimental setup and data acquisition. DLS is also acknowledged for providing access to the B16 beamline under the allocation MT20046. PG is supported by the Commonwealth Rutherford Post-Doctoral Fellowship. PG and EV are also supported with funding from the 3DbioNet. EV is grateful to the Royal Academy of Engineering for an Industrial Fellowship. The authors especially thank Dr Hani El Kadri and Dr Himadri Gupta for helpful discussions on confocal microscopy. TS and JM acknowledge support from Imagingbiopro - Network Proof of Concept Award (PoCA) and Engineering and Physical Sciences Research Council (EP/S022813/1).

Credit author statement

Jingyi Mo: Conceptualization, Methodology, Software, Formal

analysis, Investigation, Writing – original draft, Visualization. **Nathanael Leung:** Formal analysis, Methodology, Writing – original draft. **Priyanka Gupta:** Formal analysis, Methodology, Investigation, Writing – Reviewing & Editing. **Bin Zhu:** Methodology, Investigation, Writing – original draft. **Eirini Velliou:** Conceptualization, Validation, Investigation, Resources, Writing – Reviewing & Editing, Visualization, Supervision. **Tan Sui:** Conceptualization, Methodology, Formal analysis, Investigation, Resources, Writing – original draft, Supervision, Project administration, Funding acquisition.

Appendix A. Supplementary data

Supplementary data to this article can be found online at https://doi.org/10.1016/j.mtadv.2021.100184.

References

[1] A. Adamska, A. Domenichini, M. Falasca, Pancreatic ductal adenocarcinoma: current and evolving therapies, Int. J. Mol. Sci. 18 (7) (2017) 1338.
[2] R.A. Smith, K.S. Andrews, D. Brooks, S.A. Fedewa, D. Manassaram-Baptiste, D. Saslow, O.W. Brawley, R.C. Wender, Cancer screening in the United States, 2018: a review of current American Cancer Society guidelines and current issues in cancer screening, CA, Canc. J. Clin. 68 (4) (2018) 297–316.
[3] L.A. Torre, B. Trabert, C.E. DeSantis, K.D. Miller, G. Samimi, C.D. Runowicz, M.M. Gaudet, A. Jemal, R.L. Siegel, Ovarian cancer statistics, 2018, CA, Canc. J. Clin. 68 (4) (2018) 284–296.
[4] H.E. Barker, J.T. Paget, A.A. Khan, K.J. Harrington, The tumour microenvironment after radiotherapy: mechanisms of resistance and recurrence, Nat. Rev. Cancer 15 (7) (2015) 409–425.
[5] C.J. Whatcott, R.G. Posner, D.D. Von Hoff, H. Han, Desmoplasia and Chemoresistance in Pancreatic Cancer, Pancreatic Cancer and Tumor Microenvironment, Transworld Research Network, 2012.
[6] N. Dumont, B. Liu, R.A. DeFilippis, H. Chang, J.T. Rabban, A.N. Karnezis, J.A. Tjoe, J. Marx, B. Parvin, T.D. Tlsty, Breast fibroblasts modulate early dissemination, tumorigenesis, and metastasis through alteration of extracellular matrix characteristics, Neoplasia 15 (3) (2013) 249.
[7] N. Awasthi, M.A. Schwarz, R.E. Schwarz, Enhancing cytotoxic agent activity in experimental pancreatic cancer through EMAP II combination therapy, Cancer Chemother, Pharmacol 68 (3) (2011) 571–582.
[8] D.I. Dovzhanskiy, S.M. Arnold, T. Hackert, I. Oehme, O. Witt, K. Felix, N. Giese, J. Werner, Experimental in vivo and in vitro treatment with a new histone deacetylase inhibitor belinostat inhibits the growth of pancreatic cancer, BMC Cancer 12 (1) (2012) 226.
[9] K.B. Harikumar, A.B. Kunnumakkara, G. Sethi, P. Diagaradjane, P. Anand, M.K. Pandey, J. Gelovani, S. Krishnan, S. Guha, B.B. Aggarwal, Resveratrol, a multitargeted agent, can enhance antitumor activity of gemcitabine in vitro and in orthotopic mouse model of human pancreatic cancer, Int. J. Cancer Res. 127 (2) (2010) 257–268.
[10] H. Onishi, Y. Morifuji, M. Kai, K. Suyama, H. Iwasaki, M. Katano, Hedgehog inhibitor decreases chemosensitivity to 5-fluorouracil and gemcitabine under hypoxic conditions in pancreatic cancer, Cancer Sci. 103 (7) (2012) 1272–1279.
[11] K.L. Bailey, M.A. Carlson, Porcine models of pancreatic cancer, Front. Oncol. 9 (2019) 144.
[12] S. Totti, M.C. Allenby, S.B. Dos Santos, A. Mantalaris, E.G. Velliou, A 3D bio-inspired highly porous polymeric scaffolding system for in vitro simulation of pancreatic ductal adenocarcinoma, RSC Adv. 8 (37) (2018) 20928–20940.
[13] P. Gupta, S. Totti, P.A. Pérez-Mancera, E. Dyke, A. Nisbet, G. Schettino, R. Webb, E.G. Velliou, Chemoradiotherapy screening in a novel biomimetic polymer based pancreatic cancer model, RSC Adv. 9 (71) (2019) 41649–41663.
[14] P. Gupta, P.A. Pérez-Mancera, H. Kocher, A. Nisbet, G. Schettino, E.G. Velliou, A novel scaffold-based hybrid multicellular model for pancreatic ductal adenocarcinoma—toward a better mimicry of the in vivo tumor microenvironment, Front. bioeng. biotechnol. 8 (2020) 290.
[15] N. Awasthi, D. Kronenberger, A. Stefaniak, M.S. Hassan, U. von Holzen, M.A. Schwarz, R.E. Schwarz, Dual inhibition of the PI3K and MAPK pathways enhances nab-paclitaxel/gemcitabine chemotherapy response in preclinical models of pancreatic cancer, Cancer Lett. 459 (2019) 41–49.
[16] A. Courtin, F.M. Richards, T.E. Bapiro, J.L. Bramhall, A. Neesse, N. Cook, B.-F. Krippendorff, D.A. Tuveson, D.I. Jodrell, Anti-tumour efficacy of capecitabine in a genetically engineered mouse model of pancreatic cancer, PLoS One 8 (6) (2013).
[17] V. Heinemann, M. Haas, S. Boeck, Neoadjuvant treatment of borderline resectable and non-resectable pancreatic cancer, Ann. Oncol. 24 (10) (2013) 2484–2492.
[18] S. Totti, S.I. Vernardis, L. Meira, P.A. Pérez-Mancera, E. Costello, W. Greenhalf, D. Palmer, J. Neoptolemos, A. Mantalaris, E.G. Velliou, Designing a bio-inspired biomimetic in vitro system for the optimization of ex vivo studies of pancreatic cancer, Drug Discov, Today Off. 22 (4) (2017) 690–701.
[19] T.M. Blanco, A. Mantalaris, A. Bismarck, N. Panoskaltsis, The development of a three-dimensional scaffold for ex vivo biomimicry of human acute myeloid leukaemia, Biomaterials 31 (8) (2010) 2243–2251.
[20] P. Lu, V.M. Weaver, Z. Werb, The extracellular matrix: a dynamic niche in cancer progression, Int. J. Cell Biol. 196 (4) (2012) 395–406.
[21] D.I. Zeugolis, G.R. Paul, G. Attenburrow, Cross-linking of extruded collagen fibers—a biomimetic three-dimensional scaffold for tissue engineering applications, J. Biomed. Mater. Res. 89 (4) (2009) 895–908.
[22] D. Lacroix, P. Prendergast, A mechano-regulation model for tissue differentiation during fracture healing: analysis of gap size and loading, J. Biomech. 35 (9) (2002) 1163–1171.
[23] P. Prendergast, R. Huiskes, K. Søballe, Biophysical stimuli on cells during tissue differentiation at implant interfaces, J. Biomech. 30 (6) (1997) 539–548.
[24] E.G. Velliou, S.B. Dos Santos, M.M. Papathanasiou, M. Fuentes-Gari, R. Misener, N. Panoskaltsis, E.N. Pistikopoulos, A. Mantalaris, Towards unravelling the kinetics of an acute myeloid leukaemia model system under oxidative and starvation stress: a comparison between two-and three-dimensional cultures, Bioproc. Biosyst. Eng. 38 (8) (2015) 1589–1600.
[25] G. Wishart, P. Gupta, G. Schettino, A. Nisbet, E. Velliou, 3d tissue models as tools for radiotherapy screening for pancreatic cancer 94 (1120) (2021), 20201397.
[26] G. Wishart, P. Gupta, A. Nisbet, E. Velliou, G.J.C. Schettino, Novel anticancer and treatment sensitizing compounds against pancreatic cancer 13 (12) (2021) 2940.
[27] J.M. Anderson, A. Hiltner, M.J. Wiggins, M.A. Schubert, T.O. Collier, W.J. Kao, A.B. Mathur, Recent advances in biomedical polyurethane biostability and biodegradation, Polym. Int. 46 (3) (1998) 163–171.
[28] M. Szycher, Biostability of polyurethane elastomers: a critical review, J. Biomater. Appl. 3 (2) (1988) 297–402.
[29] A.J. Engler, S. Sen, H.L. Sweeney, D.E. Discher, Matrix elasticity directs stem cell lineage specification, Cell 126 (4) (2006) 677–689.
[30] D. Ansari, H. Friess, M. Bauden, J. Samnegård, R. Andersson, Pancreatic cancer: disease dynamics, tumor biology and the role of the microenvironment, Oncotarget 9 (5) (2018) 6644.
[31] T. Sui, E. Salvati, H. Zhang, K. Nyaza, F.S. Senatov, A.I. Salimon, A.M. Korsunsky, Probing the complex thermo-mechanical properties of a 3D-printed polylactide-hydroxyapatite composite using in situ synchrotron X-ray scattering, J. Adv. Res. 16 (2019) 113–122.
[32] T. Sui, E. Salvati, S. Ying, G. Sun, I. Dolbnya, K. Dragnevski, C. Prisacariu, A. Korsunsky, Strain softening of nano-scale fuzzy interfaces causes Mullins effect in thermoplastic polyurethane, Sci. Rep. 7 (1) (2017) 1–9.
[33] T. Sui, N. Baimpas, I.P. Dolbnya, C. Prisacariu, A.M. Korsunsky, Multiple-length-scale deformation analysis in a thermoplastic polyurethane, Nat. Commun. 6 (1) (2015) 1–9.
[34] C. Zhou, H. Li, W. Zhang, J. Li, S. Huang, Y. Meng, J.d. Christiansen, D. Yu, Z. Wu, S. Jiang, Direct investigations on strain-induced cold crystallization behavior and structure evolutions in amorphous poly (lactic acid) with SAXS and WAXS measurements, Polymer 90 (2016) 111–121.
[35] L. Safinia, A. Mantalaris, A. Bismarck, Nondestructive technique for the characterization of the pore size distribution of soft porous constructs for tissue engineering, Langmuir 22 (7) (2006) 3235–3242.
[36] J. Mo, N. Leung, P. Gupta, B. Zhu, H. Xing, J. Zhang, E. Velliou, T. Sui, Technology, Multi-scale structural and mechanical characterisation in bioinspired polyurethane-based pancreatic cancer model, J. Mater. Res. Technol. 15 (2021) 2507–2517.
[37] C.A. Schneider, W.S. Rasband, K.W. Eliceiri, NIH Image to ImageJ: 25 years of image analysis, Nat. Methods 9 (7) (2012) 671–675.
[38] T. Sui, E. Salvati, H. Zhang, I. Dolbnya, A. Korsunsky, Multiscale synchrotron scattering studies of the temperature-dependent changes in the structure and deformation response of a thermoplastic polyurethane elastomer, Mater. Today Adv. 4 (2019) 100024.
[39] B.D. Kaushiva, G.L. Wilkes, Influence of diethanolamine (DEOA) on structure–property behavior of molded flexible polyurethane foams, J. Appl. Polym. Sci. 77 (1) (2000) 202–216.
[40] S. D'hollander, C.J. Gommes, R. Mens, P. Adriaensens, B. Goderis, F. Du Prez, Modeling the morphology and mechanical behavior of shape memory polyurethanes based on solid-state NMR and synchrotron, SAXS/WAXD 20 (17) (2010) 3475–3486.
[41] A. Mott, G. Lenormand, J. Costales, J.J. Fredberg, B.A. Burleigh, Modulation of host cell mechanics by Trypanosoma cruzi, J. Cell. Physiol. 218 (2) (2009) 315–322.
[42] C. Rotsch, M. Radmacher, Drug-induced changes of cytoskeletal structure and mechanics in fibroblasts: an atomic force microscopy study, Biophys. J. 78 (1) (2000) 520–535.
[43] W.A. Lam, M.J. Rosenbluth, D.A. Fletcher, Chemotherapy exposure increases leukemia cell stiffness, Blood 109 (8) (2007) 3505–3508.
[44] M. Vitale, M. Illario, T. Di Matola, A. Casamassima, G. Fenzi, G.J.E. Rossi, Integrin binding to immobilized collagen and fibronectin stimulates the proliferation of human thyroid cells in culture, Endocrinology 138 (4) (1997) 1642–1648.
[45] M. Barczyk, S. Carracedo, D.J.C. Gullberg, t. research, Integr. Cell Tissue Res. 339 (1) (2010) 269–280.
[46] F. Wang, S. Chen, Q. Wu, R. Zhang, P. Sun, Strain-induced structural and dynamic changes in segmented polyurethane elastomers, Polymer 163 (2019)

154–161.
[47] F. Yeh, B.S. Hsiao, B.B. Sauer, S. Michel, H.W. Siesler, In-situ studies of structure development during deformation of a segmented poly (urethane– urea) elastomer, Macromolecules 36 (6) (2003) 1940–1954.
[49] S. Toki, I. Sics, S. Ran, L. Liu, B.S. Hsiao, Molecular orientation and structural development in vulcanized polyisoprene rubbers during uniaxial deformation by in situ synchrotron X-ray diffraction, Polymer 44 (19) (2003) 6003–6011.
[50] Y. Miyamoto, H. Yamao, K. Sekimoto, Crystallization and melting of polyisoprene rubber under uniaxial deformation, Marcomolecules 36 (17) (2003) 6462–6471.
[51] Y. Fukahori, Mechanism of the self-reinforcement of cross-linked NR generated through the strain-induced crystallization, Polymer 51 (7) (2010) 1621–1631.